nature communications

Article

https://doi.org/10.1038/s41467-024-55626-8

Spin polarization induced by atomic strain of MBene promotes the $\cdot O_2^-$ production for groundwater disinfection

Received: 26 July 2024

Accepted: 18 December 2024

Published online: 02 January 2025

Check for updates

Zhaoli Liu[1,2,6], Wenzhe Gao[1,6], Lizhi Liu[3], Yixuan Gao[2], Cui Zhang[1], Long Chen[2], Fan Lv[4], Jiafeng Xi[1], Ting Du[1], Linpin Luo[1], Junchen Zhuo[1], Wentao Zhang[1], Yanwei Ji[1], Yizhong Shen[5] ✉, Wen Liu[2] ✉, Jianlong Wang[1] ✉, Mingchuan Luo[4] & Shaojun Guo[4] ✉

Superbugs in groundwater are posing severe health risks through waterborne pathways. An emerging approach for green disinfection lies at photocatalysis, which levers the locally generated superoxide radical ($\cdot O_2^-$) for neutralization. However, the spin-forbidden feature of O_2 hinders the photocatalytic generation of active $\cdot O_2^-$, and thus greatly limited the disinfection efficiency, especially for real groundwater with a low dissolved oxygen (DO) concentration. Herein, we report a class of strained $Mo_{4/3}B_{2-x}T_z$ MBene (MB) with enhanced adsorption/activation of molecular O_2 for photocatalytic disinfection, and find the strain induced spin polarization of $In_2S_3/Mo_{4/3}B_{2-x}T_z$ (IS/MB) can facilitate the spin-orbit hybridization of Mo sites and O_2 to overcome the spin-forbidden of O_2, which results in a 16.59-fold increase in $\cdot O_2^-$ photocatalytic production in low DO condition (2.46 mg L^{-1}). In particular, we demonstrate an $In_2S_3/Mo_{4/3}B_{2-x}T_z$ (50 mg)-based continuous-flow-disinfection system stably operates over 62 h and collects 37.2 L bacteria-free groundwater, which represents state-of-the-art photodisinfection materials for groundwater disinfection. Most importantly, the disinfection capacity of the continuous-flow-disinfection system is 25 times higher than that of commercial sodium hypochlorite (NaOCl), suggesting the practical potential for groundwater purification.

Groundwater accounts for 99% of all liquid freshwater on earth and provides nearly 50% of the global population's domestic water and 25% of agricultural irrigation water, which are critical to poverty eradication, food and water security, and socio-economic development[1]. Previous studies show that groundwater, associated with many outbreaks[2], is a major global reservoir of antibiotic-resistant bacteria[3]. The waterborne diseases are a sustainable issue for the developing country[2]. Globally, water disinfection relies on chlorination, however, by-products of chlorination is linked with cancer[3]. There is a great requirement for focusing on disinfectants without chemical residue formation[4,5]. Reactive oxygen species (ROS) disinfectants, such as superoxide radical ($\cdot O_2^-$), can offer broad-spectrum antibacterial activity without chemical residues[5]. Among different techniques, photocatalysis provides a sustainable approach to produce $\cdot O_2^-$ by

[1]College of Food Science and Engineering, Northwest A&F University, 712100 Yangling, China. [2]The Key Laboratory of Water and Sediment Sciences, Ministry of Education, College of Environmental Sciences and Engineering, Peking University, 100871 Beijing, China. [3]School of Materials Science and Engineering, Northwestern Polytechnical University, 710072 Xian, China. [4]School of Materials Science and Engineering, Peking University, Beijing, China. [5]Hefei University of Technology, School of Food & Biological Engineering, 230009 Hefei, China. [6]These authors contributed equally: Zhaoli Liu, Wenzhe Gao.
✉e-mail: yzshen@hfut.edu.cn; wen.liu@pku.edu.cn; wanglong79@nwsuaf.edu.cn; guosj@pku.edu.cn

activating oxygen (O_2). However, low $\cdot O_2^-$ flux in the reported photocatalytic systems greatly limits the disinfection efficiency. Therefore, enhancing the photocatalytic ability for the $\cdot O_2^-$ production is highly desirable in photocatalytic disinfection.

O_2 is the most environmental oxidant on earth, and the activation of O_2 strengthens its reactivity[6]. For the spin distribution in the O_2 molecule, a pair of half-occupied π^* orbitals endow O_2 with nonzero spin ($s=1$; $m_z=2\mu_B$), which is the source of spin-forbidden[7,8]. If π^* orbitals obtain an electron, the spin states of O_2 will be split and transformed into $\cdot O_2^-$. However, the spin-forbidden of O_2 impedes this electron transfer, leading to the low-efficiency generation of $\cdot O_2^-$, and thus low disinfection efficiency. Till now, in low DO water, such as groundwater, how to eliminate the spin-forbidden of O_2 is the key to improving the O_2 utilization and sterilization efficiency, however, remains a grand challenge.

Herein, we report a class of 2D/2D $In_2S_3/Mo_{4/3}B_{2-x}T_z$ (IS/MB) heterojunction, in which MB as cocatalyst with atomic strain produces the spin polarization for high-efficiently generate the $\cdot O_2^-$ for boosting the disinfection efficiency in groundwater. In-situ electron paramagnetic resonance (EPR) and molecular orbital analysis reveal that spin-polarized orbitals hybridization between IS/MB-20 and O_2 can eliminate the spin-forbidden of O_2 for facilitating photoelectron transfer for efficient $\cdot O_2^-$ production. The as-made IS/MB-20 shows a 16.59-fold increase in $\cdot O_2^-$ production relative to IS and exhibits unprecedented MRSA disinfection efficiency (8.06-log reduction within 15 min under visible light irradiation). Continuous flow disinfection system equipped with 50 mg IS/MB-20 can produce 37.2 L bacteria-free water and also shows durability over 62 h, which represents state-of-the-art photodisinfection materials for groundwater disinfection. Furthermore, the continuous-flow-disinfection system's capacity for disinfection in groundwater is 25 times greater than that of commercial NaOCl.

Results

Synthesis and chemical structure of MB

$Mo_{4/3}B_{2-x}T_z$ MBene (MB) was prepared through a HF etching and delamination process of $(Mo_{2/3}Y_{1/3})_2AlB_2$ (*i*-MAB) (Supplementary Figs. 1, 2)[9]. The average thickness of as-made MB-20 (20 h HF etching) nanosheets is about 5.67 nm (Supplementary Fig. 3). The dramatical reduction in Y 3*d* and Al 2*p* X-ray photoelectron spectra (XPS) peaks of

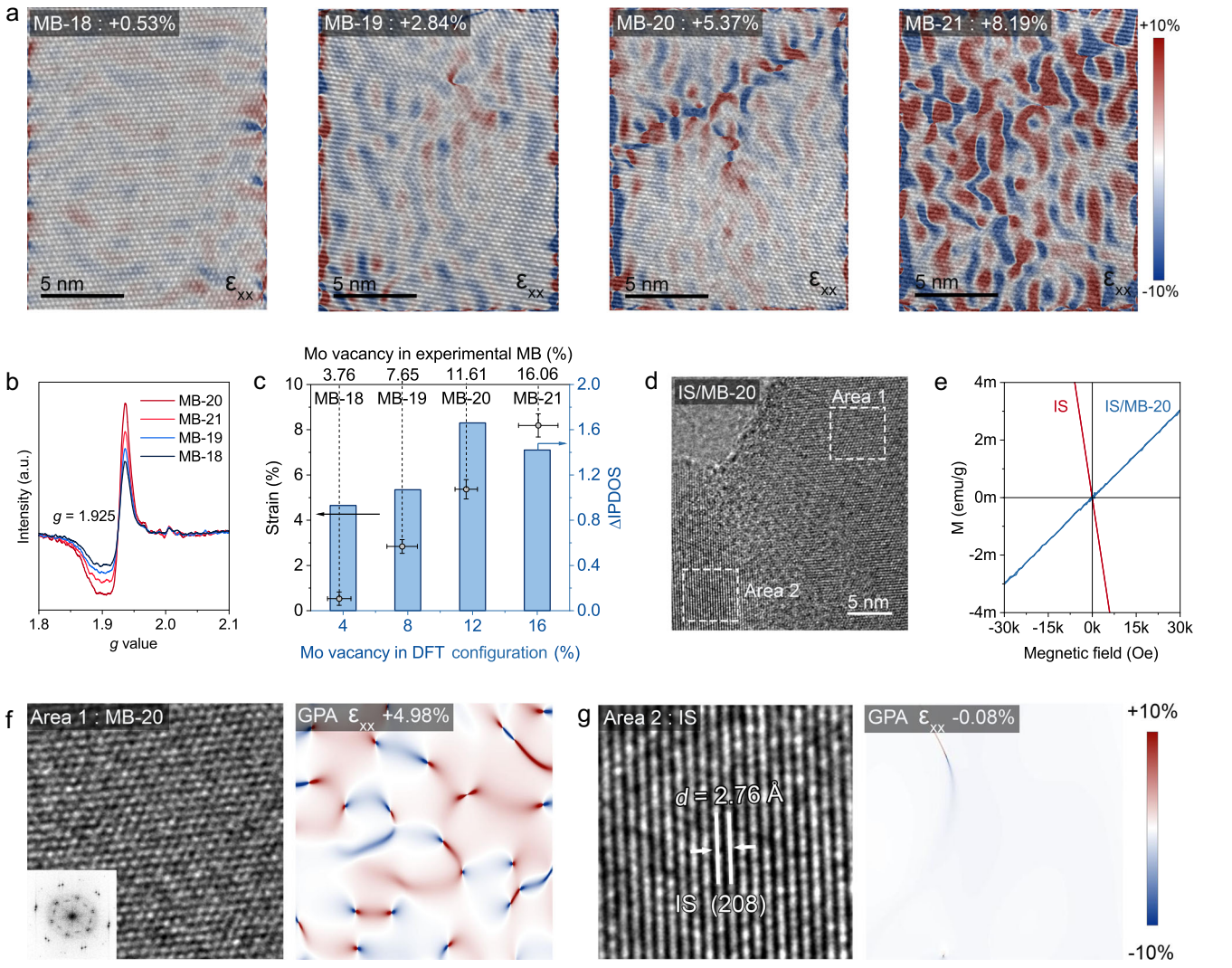

Fig. 1 | Structure characterization and structure–activity relationship between atomic strain and spin polarization. a AC-STEM and GPA images of MB with different HF etching times (18–21 h). ε_{xx} is the strain along the horizontal axis. **b** The EPR of MB-18/19/20/21. **c** Structure–activity relationship among Mo vacancy, tensile strain, and spin polarization. All error bars represent the standard deviation of three independent measurements. **d** HRTEM image of IS/MB-20. **e** Magnetic hysteresis loop of IS and IS/MB-20. **f** and **g** HRTEM images of areas 1 and 2, and corresponding strain mapping images based on GPA. The inset image in Fig. 1f is the SAED image of MB-20.

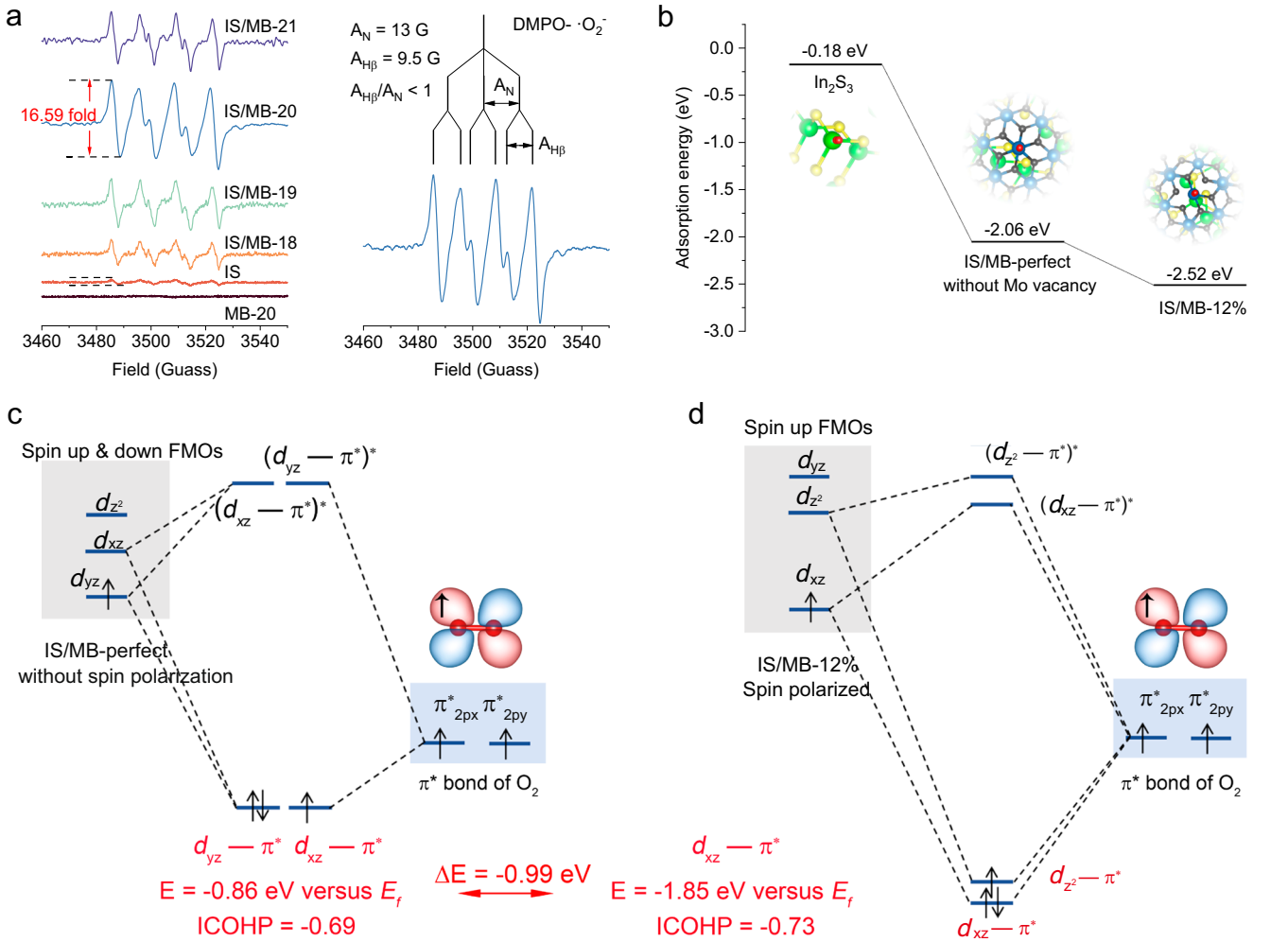

Fig. 2 | Spin polarization enhanced O_2 adsorption. a In-situ EPR spectra of·O_2^- produced by various materials in low DO condition (2.46 mg L^{-1}) under visible light irradiation. **b** Adsorption energy of O_2 on various materials. The inset figures from left to right represent the configurations of O_2 adsorption on the surface of In_2S_3, IS/MB-perfect, and IS/MB-12%. **c** Energy levels of IS/MB-perfect's FMOs and O_2's π^* orbitals. **d** Energy levels of IS/MB-12%'s FMOs and O_2's π^* orbitals.

MB-20 confirms the removal of Al and Y atoms during the MB synthesis (Supplementary Figs. 4, 5). X-ray diffraction (XRD) patterns indicate that the peak intensities of $(Mo_{2/3}Y_{1/3})_2AlB_2$ precursor are significantly decreased after the HF treatment (Supplementary Fig. 6). As a comparison, the (000*l*) peak of MB-20 shifts to a lower diffraction angle of $2\theta = 7.47°$, suggesting that the MB-20 is composed of stacked 2D sheets, with an increased *d*-spacing value (*d*) of 11.83 Å[9].

The aberration corrected-spherical transmission electron microscope (AC-STEM) image of MB-20 shows that it has a hexagonal crystal structure (Supplementary Fig. 7). The uneven brightness of atoms in Supplementary Fig. 8a indicates Mo vacancies are formed. The corresponding three-dimensional (3D) atom-overlapping Gaussian-function fitting mappings further demonstrate the formation of Mo in MB-20 formation. Moreover, the simulated STEM image of MB-20 also demonstrates a darker signal of the Mo vacancies (Supplementary Fig. 8b), in consistent with the experimental results. In the Fourier transform of Mo K-edge extended X-ray absorption fine structure (FT-EXAFS) spectra in R space (Supplementary Fig. 9), MB-20 emerges a primary peak at 1.84 Å, confirming the existence of Mo−B coordination (Supplementary Table 1). The coordination number of Mo−B in MB-20 is determined to be 6.31. Furthermore, based on crystal structure information provided by AC-STEM, FT-EXAFS, and previous study[9], we built a crystal structure model of MB-20 (Supplementary Fig. 10). The simulated electron diffraction (ED) and simulated X-ray diffraction (XRD) patterns of MB-20 model are in accordance with the experiment results (Supplementary Figs. 6, 7), supporting the validity of the established crystal structure.

Atomic strain-induced spin polarization in MB

Figure 1a shows the atomic structure and GPA result of MB with different etching times (18–21 h). MB-18 (18 h HF etching) exhibits a regular hexagonal close-packed (hcp) atomic arrangement, and GPA data indicates the existence of slight in-plane strain in MB-18 (average strain: +0.53%). As a comparison, MB-19/20/21 samples experience the tensile strain (average strain: +2.84%, +5.37%, and +8.19%, respectively)[10]. The precise control of the HF etching time is crucial for regulating the strain degree. XPS, inductively coupled plasma optical emission spectrometer (ICP-OES), and XRD results also demonstrate that MB undergoes the Mo vacancy formation and structure relaxation in the etching time of 18–21 h (Supplementary Figs. 11–13).

To reveal the effect of strain on MB's electronic structure, density functional theory (DFT) calculations were performed. Based on the concentration of Mo vacancy obtained from ICP-OES (Supplementary Fig. 12), the crystal structures of various MB with different amounts of Mo vacancy were established (Supplementary Fig. 14). Supplementary Fig. 15 shows the density of states (DOS) of MB-4%/8%/12%/16% (theoretical model representing MB-18/19/20/21). In general, the difference between the spin-up and spin-down integral DOS ($\Delta IDOS = IDOS_{spin\text{-}down} - IDOS_{spin\text{-}up}$) represents the spin polarization[11,12]. Among these MB models, MB-12%, which simulates

the MB-20 with 11.61% Mo vacancies, has a more pronounced spin polarization than other materials according to the largest ΔIDOS = 1.66 (Supplementary Fig. 15). Electron paramagnetic resonance (EPR) results are consistent with calculated spin polarization (Fig. 1b). At room temperature, all the MB materials exhibit paramagnetic character, attributed to unpaired electrons. The intensity of paramagnetic character spectra increases with increasing Mo vacancy concentration from MB-18 to MB-20, similar to other strained transition-metal 2D materials[13]. However, the magnetization is weakened when the Mo vacancy concentration is too high in MB-21. In summary, the structure–activity relationship of atomic strain and spin polarization in MB is shown in Fig. 1c. The spin-charge density of MB-12% illustrates asymmetric electron spin polarization distribution (Supplementary Fig. 16), and a large area of negative spatial spin polarization in MB-12% indicates a small possibility of spin polarization flip.

To explore the spin polarization mechanism in the strained MB, the wave function analysis was performed. In Supplementary Fig. 17, there is an obvious d–p orbital hybridization between the Mo d_{xy} orbital and the boron six-membered ring in MB. Obviously, strain weakens the orbital hybridization between Mo and B in MB-12%. To verify the rationality of theoretical calculation, we performed the soft X-ray absorption spectroscopy (XAS) analysis for all MB materials (Supplementary Fig. 18). We found that HF etching breaks the crystal structure of MB, which leads to both weakened $5s \rightarrow \sigma^*$ and $5s \rightarrow \pi^*$ signals, suggesting weaker hybridization between Mo and B orbitals[14]. Generally, when the strain changes orbitals, the orbital magnetic moment will inevitably lead to the transformation of the electron spin-state, resulting in the spin–orbit coupling[13,15]. Spin–orbit coupling is the main cause of spin polarization.

Chemical and band structures of IS/MB

The electronic band structures of MB were analyzed based on DFT calculations. Substantial electronic states crossing the Fermi level, and the conductivity test results demonstrate the metallic conductivity of MB-20, implying its exceptional capability to extract electrons from semiconductors (Supplementary Fig. 20). Therefore, MB-20 can be introduced into semiconductors to afford a Schottky heterojunction photocatalyst. In this study, In_2S_3 (IS) is selected as a model semiconductor to couple with MB-20 for heterojunction construction, and the role of MB-20 in photocatalysis is explored considering its band alignment and 2D expandable region (Supplementary Fig. 21).

IS/MB-20 heterostructure was then fabricated by a facile self-assembly method. TEM and SEM images display the basic nanoflower structure of IS/MB-20 (Supplementary Figs. 21, 22). High-resolution TEM (HRTEM) image of IS/MB-20 shows a dual-phase heterostructure (Fig. 1d). Hysteresis loop results further reflect the spin polarization in IS/MB-20. At room temperature, IS/MB-20 exhibits paramagnetic character, attributed to the introduction of strained MB-20 (Fig. 1e). In Fig. 1f, fast Fourier transform (FFT) data of Area 1 reveals a hexagonal symmetry, which could be indexed to the MB phase. GPA data further demonstrate the lattice tensile strain of Area 1 (+4.98%), which is inherited from the MB-20. As a comparison, IS shows a weak strain (−0.08%) (Fig. 1g). HRTEM results of IS/MB-20 indicate that stained MB-20 was successfully embedded into IS. And GPA data suggest that the MB-20 in IS/MB-20 composite maintains the tensile strain structure. In addition, element mapping, XRD, and XPS data further confirm the successful preparation of IS/MB-20 (Supplementary Figs. 21e, 23, 24).

The band alignments of IS/MB-20 are calculated according to experiment data (Supplementary Figs. 25–27). The different potential between IS and MB-20 induces band bending. Thus, a Schottky barrier is formed at the interface (Supplementary Fig. 27b). The Schottky barrier can prevent the photogenerated charges trapped by the electron acceptor (like MB-20) from flowing back to the semiconductor (like IS).

MB enhancing $\cdot O_2^-$ photocatalytic production

The energy level diagram reveals that IS/MB-20 can produce $\cdot O_2^-$ due to its more negative CBM position (−0.67 eV) than that of $O_2/\cdot O_2^-$ (−0.33 eV) (Supplementary Fig. 27b). Under visible light irradiation, in-situ EPR spectra of IS/MB-20 confirm the production of $\cdot O_2^-$ with a hyperfine coupling constant of $A_N = 13$ G and $A_{H\beta} = 9.5$ G (Fig. 2a). The ability for $\cdot O_2^-$ production follows the order of IS/MB-20 > IS/MB-21 > IS/MB-19 > IS/MB-18. $\cdot O_2^-$ production is related to the spin polarization intensity of MB. Moreover, IS/MB-20 exhibits a stronger EPR signal than IS (16.59-fold increase), indicating it has a stronger ability to produce the $\cdot O_2^-$ under visible light irradiation.

To verify the promoting effect of MB in photocatalytic $\cdot O_2^-$ generation, the photogenerated charge carrier separation and change lifetime were investigated. The ground state bleaching (GSB) signals of IS/MB-20 are stronger than those of IS, indicating more efficient carrier dynamics in IS/MB-20 than in IS (Supplementary Figs. 28, 29). Transient photocurrent responses, surface photovoltage, and fluorescence emission decay spectra results also provide solid evidence for this claim (Supplementary Fig. 30)[16,17]. The efficient charge separation can be attributed to the Schottky barrier at the hetero-interface, which facilitates the photocatalytic $\cdot O_2^-$ production.

The charge dynamics results obtained from in-situ XPS suggest that electrons accumulate on Mo atoms of IS/MB-20 during photocatalysis (Supplementary Fig. 31). Thus, $\cdot O_2^-$ is mainly generated on Mo sites after gaining the electrons. Charge density difference and Bader charge analysis results indicate electrons transfer from Mo to O atom and also confirm the activation of O_2 on the Mo sites (Supplementary Figs. 32, 33). The adsorption energies of O_2 on different materials are calculated and presented in Fig. 2b. O_2 is more likely adsorbed on IS/MB-12% configuration ($E_{ads} = -2.52$ eV) than IS/MB-perfect ($E_{ads} = -2.06$ eV) and IS ($E_{ads} = -0.18$ eV) due to the more negative adsorption energy[18]. These results suggest that spin polarization improves the adsorption of O_2 on the material's surface.

Molecular orbital theory is further employed to analyze the orbital interaction of Mo and O_2. Projected density of states (PDOS) in Supplementary Fig. 34 shows that s–s and s–p orbitals are overlapped between Mo and B, thus enabling the formation of σ bonds. Generally, FMOs have higher reactivity than other orbitals[19]. The FMOs of IS/MB-12% are mainly composed of Mo $4d_{xz}$, Mo $4d_{z^2}$, and Mo $4d_{yz}$ orbitals (Supplementary Figs. 35–38). In addition, the hexahedral configuration of MB gives it C_{6v} symmetry. Based on the incommensurable representation of the C_{6v} point group and crystal field theory, the orbital interaction between Mo and B is shown in Supplementary Fig. 39. Obviously, the Mo $4d_{xz}$, Mo $4d_{z^2}$, and Mo $4d_{yz}$ constitute the FMO of Mo, in consistent with the PDOS results in Supplementary Fig. 34.

During O_2 adsorption and activation, the $\pi^*_{2p_x}$ and $\pi^*_{2p_y}$ bonds of O_2 can interact with the FMOs of IS/MB-12%, because these orbitals are not fully occupied (Supplementary Fig. 40). Then PDOS spectra reveal the orbitals hybridization between FMOs of IS/MB and π^* orbitals of O_2 (Supplementary Fig. 41). In addition, projected crystal orbital Hamilton population (pCOHP) analysis demonstrates the Mo $4d_{yz}$–O $2p_y$, and Mo $4d_{xz}$–O $2p_x$ orbital hybridization states (Supplementary Fig. 42). Figure 2c, d and Supplementary Fig. 43 summarize the orbital hybridization energy levels between FMOs of IS/MB and π^* orbitals of O_2 based on PDOS and pCOHP results. Obviously, the spin-polarized FMOs in IS/MB-12% exhibit a strong coupling character to O_2's π^* orbitals, thus reducing the O_2 adsorption energy[19]. After O_2 is absorbed on IS/MB-perfect, Mo $4d_{xz}$–π^* and Mo $4d_{yz}$–π^* bonds are formed and located at −0.86 eV. As a comparison, after FMOs of IS/MB-12% are hybridized with O_2's π^* orbitals, Mo $4d_{xz}$–π^* and Mo $4d_{z^2}$–π^* bonds are formed with spin energy splitting. Specifically, the spin-down Mo $4d_{xz}$–π^* and Mo $4d_{z^2}$–π^* bonds remain at the same level ($E = -1.72$ eV), while the spin-up Mo $4d_{xz}$–π^* and Mo $4d_{z^2}$–π^* bonds are located at −1.85 and −1.68 eV, respectively. In addition, for IS/MB-perfect, the integrate pCOHP (ICOHP) of spin up/down Mo $4d_{yz}$–O $2p_y$ and

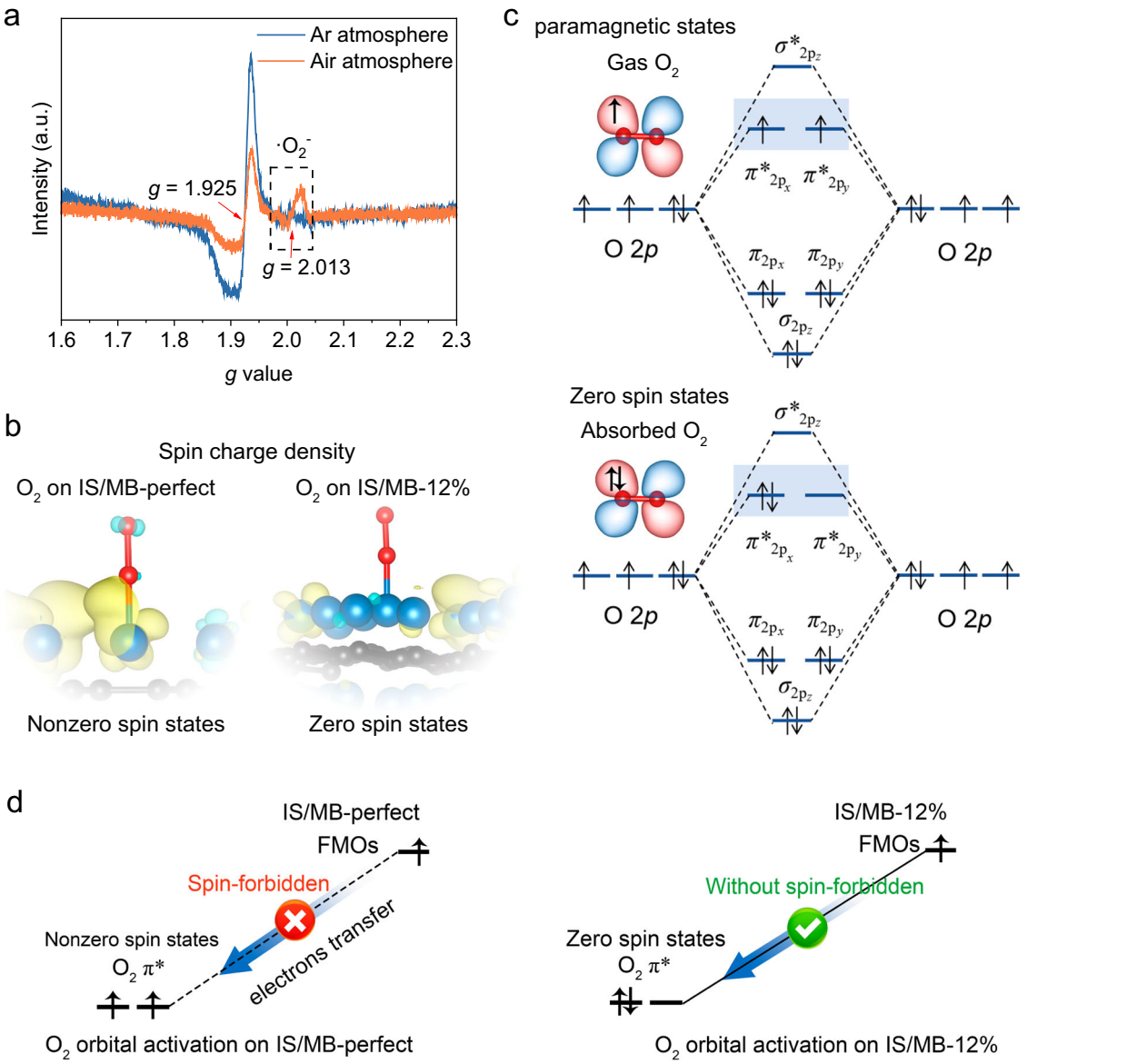

Fig. 3 | Spin polarization improving the molecular orbital activation in $\cdot O_2^-$ formation. a EPR spectra of IS/MB-20 in an Ar/Air atmosphere under light irradiation. **b** Spin charge density of IS/MB-perfect-O_2 and IS/MB-12%-O_2 configuration. **c** The molecular orbital energy and spin electron distribution diagram for O_2 and zero spin states O_2. **d** Schematic diagram of spin electron transfer from FMOs of IS/MB to π^* orbitals of O_2.

Mo $4d_{xz}$–O $2p_x$ bonds are −0.69. In contrast, the ICOHP of Mo $4d_{z^2}$–O $2p_x$ bond shifts to −0.73 in IS/MB-12%-O_2, indicating stronger bonding than IS/MB-perfect. The different energy levels and bonding strengths of Mo–O bonds are mainly attributed to different spin-orbital hybridization during O_2 adsorption[19], and the spin–orbital hybridization in IS/MB-12%-O_2 facilitates spin state transformation of O_2. Supplementary Fig. 44 presents the real space orbital wave-functions post-interaction of IS/MB-perfect-O_2 and IS/MB-12%-O_2 (with O_2 adsorbed) configuration, respectively. Generally, the overlapping of orbital wave-functions represents orbital hybridization[19]. The FMOs exhibit obvious orbital overlapping with O_2's π^* orbitals, which is consistent with the energy levels diagram in Fig. 2c and d.

Supplementary Fig. 45 displays the orbits and electron arrangement in $\cdot O_2^-$. The mechanism of $\cdot O_2^-$ formation is filling the π^* orbitals with an electron, however, the spin-forbidden nature of O_2 hinders this electron transfer. To investigate the electron transfer between Mo sites and O_2, the EPR measurements on IS/MB-20 in the Ar/Air atmosphere under light irradiation were conducted (Fig. 3a). In the Ar atmosphere, IS/MB-20 exhibits the existence of unpaired electrons. However, in the Air atmosphere, the intensity of unpaired electrons signal of IS/MB-20 is reduced, indicating the number of spins is reduced after O_2 adsorption. This suggests that the O_2 can withdraw spin electron density from Mo active sites. In addition, a new weak peak with $g = 2.013$ is observed under the illumination of IS/MB-20, suggesting the generation of $\cdot O_2^-$. Interestingly, the spin-charge density data demonstrate the spin state transformation of O_2 after adsorption on IS/MB-12% (Fig. 3b), as the O_2 molecule on IS/MB-12% shows less spin-charge density than that on the IS/MB-perfect configuration, indicating the spin degeneracy. This spin state transformation indicates spin electron rearrangement in π^* orbitals and eventually leads to the zero spin states (Fig. 3c). As mentioned above, spin-polarized FMOs coupled with O_2's π^* orbital will lead to the formation of strong Mo–O bonds (Fig. 2d and Supplementary Fig. 43). The rearrangement of the energy levels can facilitate spin electron redistribution, and result in zero spin states[20]. Furthermore, the zero-spin state eliminates the spin-forbidden and thus promotes the generation of $\cdot O_2^-$ (Fig. 3d).

Photocatalytic disinfection activity of IS/MB

Methicillin-resistant *Staphylococcus aureus* (MRSA) is a common superbug, which causes bacterial infections in healthcare and community environment[21,22]. Coagulases of MRSA allow it to proliferate as thromboembolic lesions and are hard to kill, causing a serious infection[23–26]. In addition, MRSA belongs to Gram-positive bacteria. The cell wall of Gram-positive bacteria is composed of peptidoglycan, which prevents the ROS produced by photocatalysis from penetrating the cell wall to attack bacterial cells. Therefore, MRSA, a common antibiotic-resistant bacterium, has a higher greater threat to humanity. Therefore, we choose MRSA as our target. Figure 4a shows no significant MRSA colony-forming units (CFU) reduction was observed for all materials under dark conditions, indicating a weak disinfection effect. However, under 15 min of visible light irradiation, an 8.06-log reduction of CFU was observed after incubating with IS/MB-20. The higher antibacterial performance of the IS/MB-18/19/20/21 than the IS group, demonstrating that MB cocatalyst can enhance the photocatalytic sterilization property (Fig. 4a and Supplementary Fig. 46). To the best of our knowledge, the developed IS/MB-20 is the most efficient photocatalytic disinfection material against MRSA ever reported (Fig. 4b and Supplementary Table 2).

Furthermore, the live/dead fluorescence staining was used to examine the bactericidal activity against MRSA (Fig. 4c). After staining, live and dead bacteria with intact and ruptured cell membranes exhibit green and red fluorescence, respectively. The percentage of red fluorescence significantly rose to ~98% in the IS/MB-20 group, suggesting superior antibacterial activity[27]. As a comparison, a weak bactericidal effect is observed in the group of IS under light illumination, also demonstrating the key role of MB-20 in photocatalytic sterilization.

The ROS scavenging tests suggest that $\cdot O_2^-$ is essential for the photocatalytic inactivation of MRSA (Supplementary Fig. 47)[2], as almost no MRSA is inactivated in the presence of $\cdot O_2^-$ scavenger (1,4-benzoquinone). Disinfection activity of materials is in the order of IS/MB-20 > IS/MB-21 > IS/MB-19 > IS/MB-18 > IS > MB-20, which is similar to the trend of the photocatalytic $\cdot O_2^-$ production (Fig. 2a). Then, we tested the intracellular ROS production capacity of IS/MB-20 treated bacteria by fluorescent ROS probe (DCFH-DA). As shown in Supplementary Fig. 48, without light irradiation, MRSA in three groups showed weak green fluorescence, suggesting low ROS levels in cells[28]. However, compared with MRSA in dark groups, the fluorescence signals of MB-20, IS, and IS/MB-20 group after light treatment were significantly enhanced, indicating that the ROS content in MRSA cells was greatly enhanced under light illumination, which can be ascribed to oxidative stress induced by photocatalytic processes[29]. Furthermore, the IS/MB-20 group exhibited the most pronounced fluorescence signal following light exposure, suggesting that the ROS levels in MRSA cells were elevated and oxidative stress was markedly evident. Oxidative stress can cause physiological and biochemical dysfunction of MRSA cells and reduce their infectivity, which is consistent with the results of transcriptomic analysis in the next section.

SEM images in Supplementary Fig. 49 show that the bacterial membrane was severely damaged by IS/MB-20 under light irradiation. Thus, $\cdot O_2^-$ can destroy the bacterial membrane and affect its permeability (Supplementary Fig. 50). The bacterial membrane potential assay and total protein determination results further prove that $\cdot O_2^-$ can destroy cell membranes (Supplementary Figs. 51, 52)[30]. In addition, comparable antibacterial efficacy was observed in Gram-negative and antibiotic-sensitive *Escherichia* coli (*E. coli*). In detail, a significant improvement was observed in the disinfection performance for IS/MB compared to the control, MB-20, and IS groups. In addition, after 15 min visible light, the sterilization activity of IS/MB is in the order of IS/MB-20 > IS/MB-21 > IS/MB-19 > IS/MB-18 > IS > MB-20, which is consistent with the inactivation effect of MRSA. Furthermore, after visible light irradiation, the 99% attenuation of green fluorescence in IS/MB-20 group indicates that IS/MB-20 exhibits a significant inactivation effect on *E. coli*. These findings elucidate the broad-spectrum antibacterial activity of IS/MB-20 (Supplementary Fig. 53).

Inhibition of MRSA's infectivity

The schematic diagram in Supplementary Fig. 54 describes that coagulase secreted from MRSA can promote the binding between MRSA cells, which favors and evades the opsonistic phagocytic clearance of host immune cells. Coagulase is the core virulence factor of MRSA in the process of wound infection[21,22,31]. After photocatalytic sterilization using IS/MB-20, MRSA cannot coagulate lyophilized plasma, indicating that MRSA bacteria cannot produce coagulase (Fig. 4d). This is compelling evidence that IS/MB-20 influences MRSA infection activity. Transcriptomic analysis reveals the apparent effect of IS/MB-20 on the gene expression of MRSA (Supplementary Fig. 55). IS/MB-20 treatment group has 448 differentially expressed genes (DEGs) in total (251 genes are up-regulated and 197 genes are down-regulated) relative to the control group. Figure 4e displays a significant color distinction between the control group and the IS/MB-20 treatment group, indicating the persistence of up- or down-regulated expression of DEGs between different samples in the group. Gene Ontology (GO) enrichment analysis and Kyoto Encyclopedia of Genes and Genomes (KEGG) pathway enrichment analysis further prove that photocatalytic treatment using IS/MB-20 greatly affects MRSA's fundamental metabolic process, which will limit its coagulase formation (Supplementary Figs. 56–59)[32–34].

The aforementioned findings support our theoretical framework regarding IS/MB-20's capacity to inhibit the viability and infection activity of MRSA (Supplementary Fig. 60). Furthermore, a rat wound infection model with MRSA (1×10^8 CFU mL^{-1}) was constructed to investigate the inhibiting MRSA infection performance of IS/MB-20 (Supplementary Figs. 61–66). IS/MB-20 can heal the MRSA-infected wounds in the established rat model within 10 days (Fig. 4f). In addition, a large amount of MRSA strain lived on the wounds of the control group after 2 days of infection. In comparison, the IS/MB-20 group exhibits negligible viable MRSA strain (Supplementary Fig. 63). These data demonstrate the inhibition of IS/MB-20 on MRSA infection.

Photocatalytic disinfection of groundwater

Due to the low dissolved oxygen content in groundwater, it is difficult to produce $\cdot O_2^-$. The key to improving the disinfection effect is to enhance the O_2 adsorption/activation of the bactericidal material. Herein, we tested the disinfection effect of the IS/MB-20 in groundwater. Figure 5a demonstrates that the DO content in groundwater is 1.46–2.21 mg L^{-1}, which is lower than that in tap water (7.54–10.19 mg L^{-1}). In addition, we designed an IS/MB-20-based water disinfection continuous flow system (Fig. 5b, Supplementary Fig. 67a), which can achieve 100% photocatalytic disinfection of bacteria on-site in water from groundwater with low DO (Fig. 5c, Supplementary Fig. 67b). It is important to note that practical water disinfection test was carried in the ambient conditions of (34°18′ N; 107°9′ E). To standardize the tests, the parameters are set by the standard ambient temperature and pressure (SATP), which are 22 °C and 1.013 bar, respectively. The stability of the continuous flow system was certificated over 62 h, and produced 37.2 L bacteria-free water under the condition of the flow rate of water: 10 mL min^{-1}; catalyst mass, 50 mg (Fig. 5d). The results of inductively coupled plasma-mass spectrometry (ICP-MS) detection showed negligible changes of In and Mo concentrations in the water samples before and after photocatalytic disinfection (Supplementary Fig. 68a), suggesting that IS/MB-20 exhibited good stability and would not affect water quality. In addition, after photocatalytic reaction, the IS/MB-20 maintained the morphology of nano-flowers, further confirming its high stability (Supplementary Fig. 68b). This exceptional stability of IS/MB-20 exceeds other top photocatalytic materials reported, which represents state-of-the-

https://doi.org/10.1038/s41467-024-55626-8

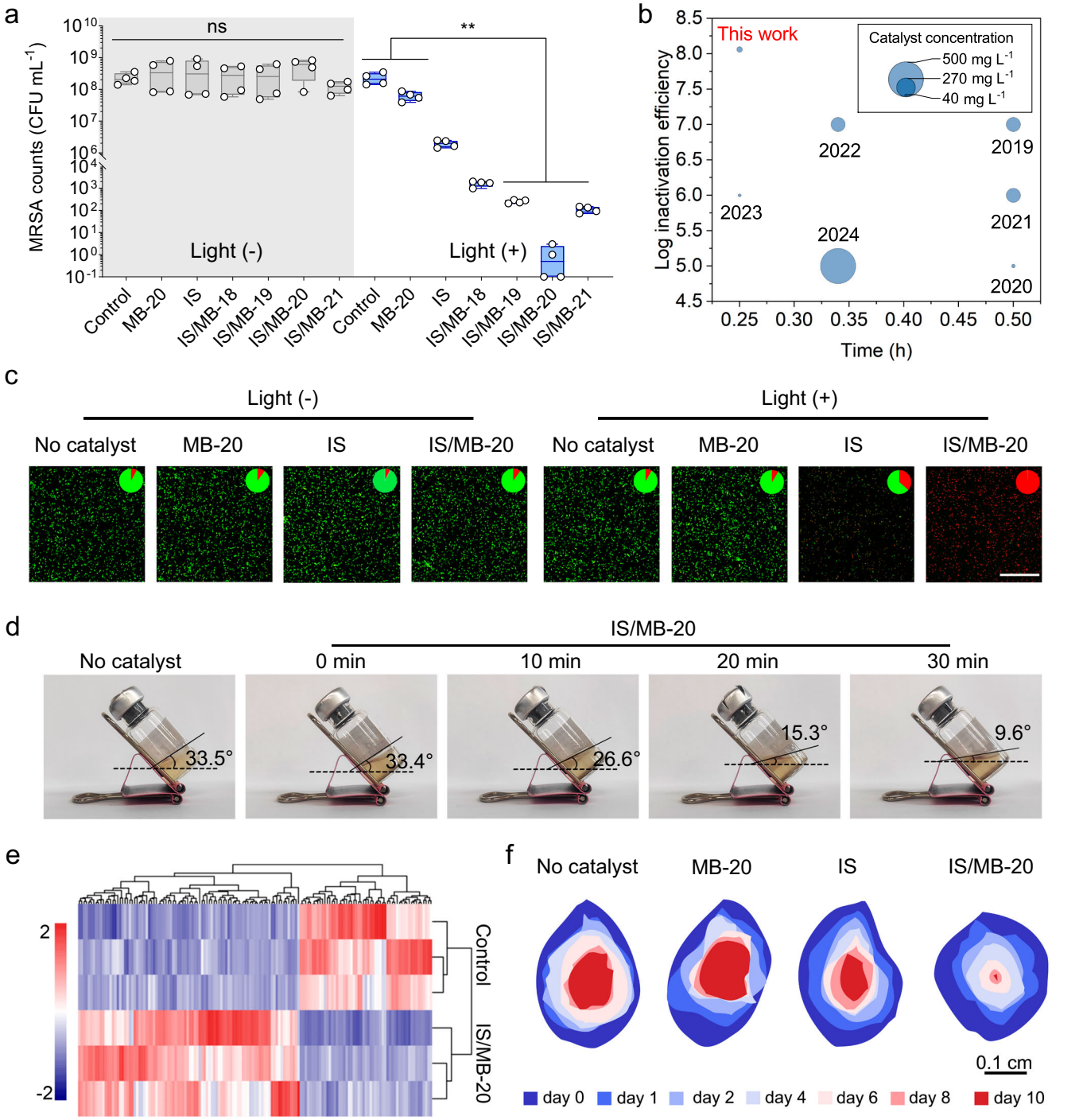

Fig. 4 | Antibacterial activities of IS/MB. a Quantitative analysis of bacterial colonies for various materials against MRSA after 15 min visible light ($\lambda \geq 420$ nm, 110 mW cm^{-2}) irradiation. No catalyst was added to the bacterial solution of the control group. Data are presented as mean ± s.d. ($n = 4$). The measurements of bacterial colonies were taken from distinct samples. Data are shown as box-and-whisker plots, with the median represented by the central line inside each box, the 25th and 75th percentiles represented by the edges of the box, and the whiskers extending to the most extreme data points. **b** Activity comparison of IS/MB-20 with reported state-of-art photocatalysts against MRSA. The inset image in Fig. 1b is the ruler of the bubble. **c** CLSM overlay projections of live (green fluorescent) and dead (red fluorescent) bacteria. The percentages of green and red fluorescent are plotted in the images. Scale bar: 50 μm. **d** Coagulase assay of MRSA treated with IS/MB-20 at different times. **e** Clustering heatmap for expression changes of DGEs. Red represents high expression of genes in the sample, and blue represents low expression. **f** Size of the MRSA-infected wound of mice during treatment with different materials for 10 days. Data are presented as mean ± standard deviations from a representative experiment ($n = 3$ independent samples). *P*-values were analyzed by a one-way ANOVA test.

art photo-disinfection materials for practical water disinfection (Fig. 5e)[35–53].

In order to evaluate the practical application potential of the system, we compared it with the bactericidal capacity of commercial NaOCl. Generally, chlorine-derived disinfectants exhibit high disinfection efficiency only over extended contact times. Therefore, we extended the sterilization time to 62 h, consistent with the IS/MB-20 disinfection test. Under the same conditions (37.2 L groundwater, 22 °C and 1.013 bar), 100% sterilization efficiency was achieved until the dosage of NaOCl reached 1250 mg (Fig. 5f). Above all, the

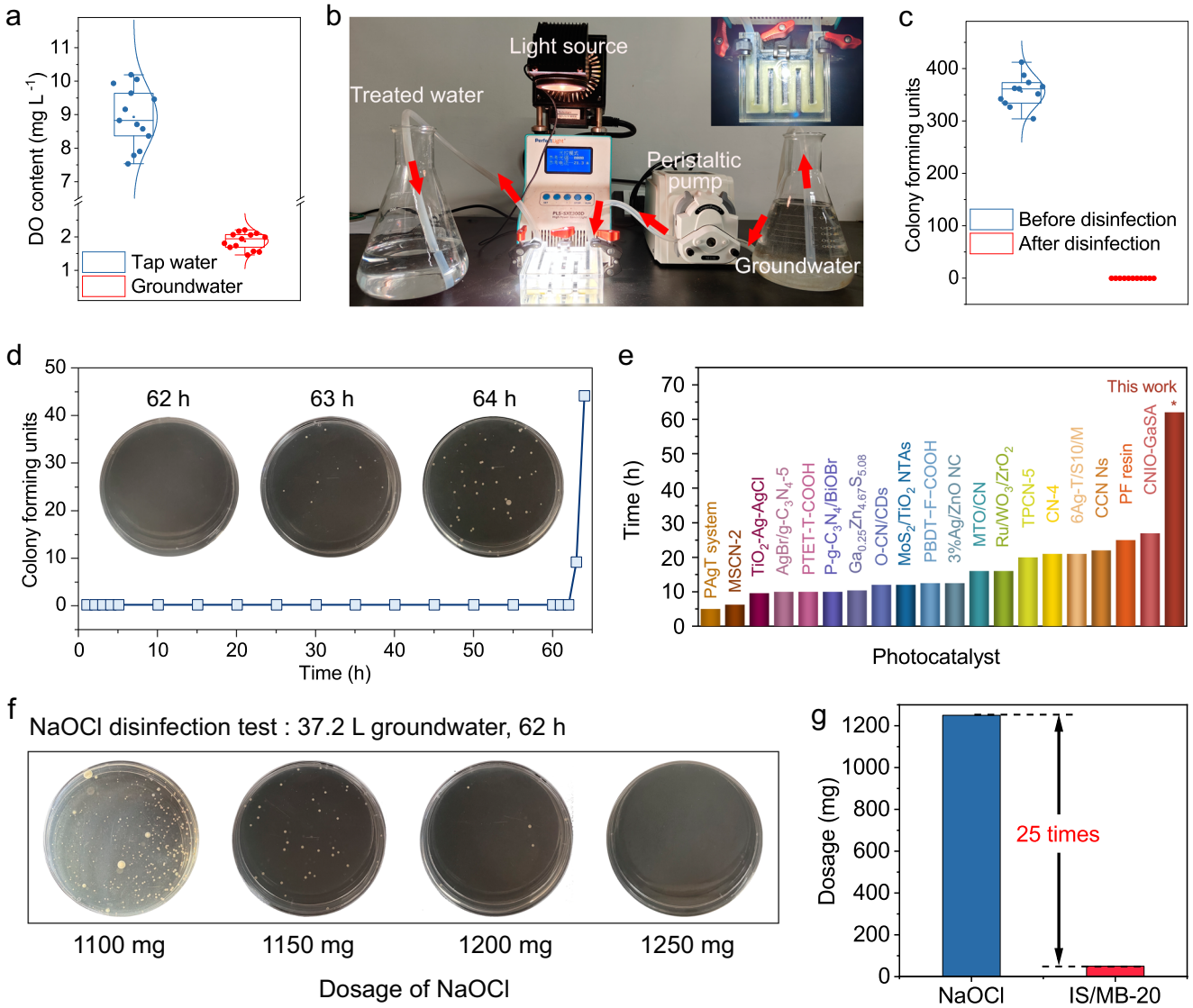

Fig. 5 | Disinfection performance of IS/MB-20 in groundwater with low DO content. a DO content of tap water and groundwater ($n = 13$). The measurements of DO content were taken from distinct samples. **b** Photograph of the continuous flow photocatalytic disinfection. **c** Groundwater disinfection performance ($n = 11$) of the continuous flow system. The measurements of bacterial colonies were taken from distinct samples. **d** Stability of the continuous flow system. The inset images are the plating photographs of water samples after 62, 63, and 64 h photocatalytic disinfection. **e** Stability comparison of IS/MB-20 with other photocatalysts reported. **f** Plating photographs showing the disinfection effect of different dosages of NaOCl in 37.2 L groundwater. **g** Dosage of NaOCl and IS/MB-20 required to produce 37.2 L of bacteria-free water. Data are shown as box-and-whisker plots, with the median represented by the central line inside each box, the 25th and 75th percentiles represented by the edges of the box, and the whiskers extending to the most extreme data points.

disinfection capability of IS/MB-20-based continuous flow system is 25.0 times that of commercial sodium hypochlorite (NaOCl) disinfectant (Fig. 5g).

Discussion

We report a class of strained MB/IS composite photocatalysts for eliminating the spin forbidden of O_2 to boost the $\cdot O_2^-$ photocatalytic production to achieve efficient water disinfection. Ascribed to its optimal tensile strain, IS/MB-20 exhibits outstanding ability for photocatalytic $\cdot O_2^-$ production. We find that the strain-induced spin-polarized FMO can hybridize with π^* orbital of O_2 to eliminate the spin forbidden of O_2, which leads to the unprecedented photocatalytic disinfection performance (15 min, 8.06-log reduction of MRSA). Moreover, an IS/MB-20-based continuous flow system can produce 37.2 L bacteria-free water with high durability of over 62 h. The system is 25 times more capable of sterilizing groundwater than commercial NaOCl. This study highlights the significance of rational tensile strain engineering in MBene cocatalyst to improve the performance of photocatalytic water disinfection in low DO conditions.

Methods

Materials and reagents

All chemicals used are commercially available and were used without any additional purification steps. $(Mo_{2/3}Y_{1/3})_2AlB_2$ (*i*-MAB, FoShan Xinxi Technology Co. Ltd.), hydrofluoric acid (HF, 40 wt%), tetrabutylammonium hydroxide (TBAOH, 10 wt%), Indium chloride tetrahydrate ($InCl_3$, 99.9%), ethylene glycol (EG, >99%), Thioacetamide (≥99.0%).

Preparation of MB

1 g of $(Mo_{2/3}Y_{1/3})_2AlB_2$ precursor was gently introduced into 20 mL of HF acid, and then magnetically stirred for 18, 19, 20, and 21 h at room temperature (25 °C), respectively. The resultant suspension was then transferred to a 50 mL centrifuge tube, and centrifugally washed

(4025×*g*, 5 min) multiple times with degassed deionized (DI) water to eliminate the leftover acid until the supernatant became neutral. Then, the precipitation obtained by the previous step of centrifugation will be further intercalated and delamination.

Synthesis of IS/MB

10 mL TBAOH was added to the precipitation and shaken for 3 min. The mixture was centrifuged (2795×*g*, 5 min) to remove the supernatant. Ethanol and water were added to the centrifuge tube to centrifugal wash away residual TBAOH (5000 rpm for 5 min, repeated 3 times), respectively. Finally, 20 mL DI water was added to the precipitation, which was shaken for 20 min. The solution was then centrifuged at 3000 rpm for 5 min to obtain colloidal suspension. The suspension was the colloidal dispersion of MB-18, MB-19, MB-20, and MB-21 sheets, respectively.

1.14 mL of 28.0 wt% ammonia solution was added into 20 mL colloidal dispersion of MB sheets. Then, 0.18 g of ammonium hydrogencarbonate solution (in 2.28 mL DI water) was added dropwise, accompanied with the formation of floccule. Afterward, the MB floccule was freeze-dried (−30 °C, 6 h) and then annealed at 150 °C in Ar atmosphere for 10 h to obtain MB powders[54].

Preparation of IS nanoflowers and IS/MB

For the preparation of IS, 0.1769 g $InCl_3$ was dissolved in 30 mL EG, followed by the addition of 0.1202 g thioacetamide. After magnetically stirring for 40 min, the mixture was poured into a 50 mL Teflon-lined reactor, and heated at 180 °C for 24 h. The obtained IS precipitate was washed with DI water and ethanol three times. Then, pure IS was obtained by drying at 80 °C for 12 h in an oven. For the IS/MB synthesis, 200 mg of pure IS was re-dissolved in 30 mL DI water. Then, 1 mL 0.3 M MB sheets colloidal dispersion was added to the IS solution, and stirred for 6 h to get IS and MB self-assembly. The obtained IS/MB precipitate was washed and dried under the same conditions to obtain pure IS/MB powder.

Characterizations

The defined morphology and composition of the materials were obtained using SEM (S-4800 FE-SEM). Elemental composition and oxidation state were obtained on X-ray photoelectron spectroscopy (ThermoFisher Scientific 250Xi, USA). All the binding energies were calibrated by the C 1*s* peak located at 284.8 V. Similar conditions were used for in-situ irradiation XPS measurements, while light irradiation was introduced. A high-resolution transmission electron microscope (HRTEM) was performed on the JEOL JEM-2100 F transmission electron microscope. The aberration-corrected high-angle annular dark-field scanning transmission electron microscopy (AC-HAADF-STEM) images were obtained on Titan Cubed Themis G2 200. XAFS tests were performed at the 1W1B station in BSRF (Beijing Synchrotron Radiation Facility, China). Femtosecond transient absorption spectra (fs-TAS) were detected by using a pump-probe system (Femto-TA100). UPS spectra were obtained on a PHI5000 VersaProbe III (Spherical Analyzer). A JEOL JES-FA200 electron spin resonance (EPR) spectrometer was used to detect the signals of the free radicals under 300 W Xenon Arc light.

Geometric phase analysis

Geometric phase analysis is a digital signal processing method for quantifying displacements and strain fields at atomic resolution. In this study, we utilized an FRWR tools plugin from the Humboldt University of Berlin, which can be plugged into the DigitalMircograph (Gatan) software to establish the strain mapping of HRTEM images in Fig. 1. Then, an in-plane strain (ε_{xx}) field is obtained to show the strain distribution.

In-situ EPR test

In situ light excitations EPR experiments were recorded on an EMXplus-6/1 EPR spectrometer (Bruker, Germany) equipped with an Xe light system, and the EPR spectrometer was operated at an X band frequency of 9.84 GHz. The spectra were obtained through rigorous monitoring to ensure that signal saturation from the applied microwave power did not occur during the acquisition of the signals. We introduced catalyst powder into a quartz tube without removing the powder sample throughout all ESR measurements, including both dark and light irradiation conditions. Prior to conducting various gas flows for in situ analysis, the quartz tube was evacuated and purged with nitrogen flow for 1 h to eliminate surface-adsorbed molecules. Under this controlled experimental setup, we were able to minimize peak variations caused by differences in the sample tube or the position of light irradiation.

In vitro antibacterial test

A 300 W Xenon Arc light (PEC2000 light Beijing Perfectlight Technology Co., Ltd., China) with a 420 nm UV cut-off filter was placed at a 40 cm distance over the reactor. The light intensity in the reactor's center was 100 mW cm^{-2}. The in vitro antibacterial system of *Escherichia coli* ATCC 25922 (*E. coli*) and Methicillin-resistant *Staphylococcus aureus* (MRSA) was studied using plate count assays. First, a single colony of *E. coli* or MRSA was picked up in lysogeny broth (LB) and cultured at 37 °C overnight. The bacteria suspension was washed and diluted with a phosphate-buffered solution (PBS). Its OD-600nm was adjusted so as to obtain a cell density, corresponding to 9 log CFU mL^{-1}, which was confirmed by plating on LB agar plates. Then, 200 μL of 800 mg L^{-1} different material solutions (the same amount of PBS solution in the control group) were added into 1.8 mL bacterial suspension and fully mixed. Afterward, the suspension was irradiated under the Xenon light. Finally, 100 μL of treated bacterial suspension was spread on a fresh LB agar plate and incubated for 18 h at 37 °C. By dividing the CFU counts of the various treatment groups by that of the control group, the survival rate was calculated.

Fluorescence imaging of generated ROS in MRSA

ROS generation in MRSA was tested using a ROS assay kit (Beyotime, China). MRSA cells (10^9 CFU mL^{-1}) were loaded with the fluorescence probe (DCFH-DA) at 37 °C for 30 min. Then the bacteria were incubated with 50 μg mL^{-1} photocatalysts and exposed to visible light for 4 min. Images of fluorescence were captured using the fluorescence microscope (LECIA TCS SP8).

Computational calculation methods

DFT calculations were carried out by the VASP.6.4.2 code. The exchange-correlation interaction was described by the GGA with the PBE functional. The energy cut-off and Monkhorst–Pack *k*-point mesh were set at 500 eV and 3 × 3 × 1, respectively. During the geometry relaxation, the convergence tolerance was set as 1.0×10^{-5} eV for energy and 0.01 eV/Å for force. The NEDOS and KPOINTS of DOS calculations were set as 800 and 5 × 5 × 1, respectively. The projected density of states (PDOS) was implemented using vaspkit code[55]. In addition, the NBANDS and NEDOS of crystal orbital Hamilton populations (COHP) calculations were set as 1500 and 1000, respectively. COHP analysis was performed using the LOBSTER 4.1.0 package[56].

Statistical analysis

All the quantitative data in each experiment were evaluated and analyzed by one-way analysis of variance and expressed as the mean values ± standard deviations. Values of $^{*}P < 0.05$, $^{**}P < 0.01$, and $^{***}P < 0.001$ were considered statistically significant.

Reporting summary

Further information on research design is available in the Nature Portfolio Reporting Summary linked to this article.

Data availability

The data that support the findings of this study are included in the Main text and the SI files. Raw data are available from the corresponding authors upon request. The Source data generated in this study are provided in the Source Data file. Source data are provided with this paper.

Code availability

The Vienna ab initio Simulation Package (VASP) for the density functional theory calculations is available at https://www.vasp.at. We used the VASPKIT.1.3.0 code and Lobster 5.1.0 code for post-processing of the VASP calculated data. And the VASPKIT.1.3.0 code and Lobster 5.1.0 code are available at Overview—VASPKIT 1.5 documentation and COHP—Crystal Orbital Hamilton Population • COHP (rwth-aachen.de), respectively.

References

1. Ferraro, P. J. & Prasse, C. Reimagining safe drinking water on the basis of twenty-first-century science. *Nat. Sustain.* **4**, 1032–1037 (2021).
2. Wu, T. et al. Solar-driven efficient heterogeneous subminute water disinfection nanosystem assembled with fingerprint MoS_2. *Nat. Water* **1**, 462–470 (2023).
3. Mitch, W. A., Richardson, S. D., Zhang, X. & Gonsior, M. High-molecular-weight by-products of chlorine disinfection. *Nat. Water* **1**, 336–347 (2023).
4. Jeon, I., Ryberg, E. C., Alvarez, P. J. J. & Kim, J.-H. Technology assessment of solar disinfection for drinking water treatment. *Nat. Sustain.* **5**, 801–808 (2022).
5. Richards, T. et al. A residue-free approach to water disinfection using catalytic in situ generation of reactive oxygen species. *Nat. Catal.* **4**, 575–585 (2021).
6. Shi, Y. et al. Surface boronizing can weaken the excitonic effects of BiOBr nanosheets for efficient O_2 activation and selective NO oxidation under visible light irradiation. *Environ. Sci. Technol.* **56**, 14478–14486 (2022).
7. Peng, J. B. et al. Atomically resolved single-molecule triplet quenching. *Science* **373**, 452–456 (2021).
8. Montemore, M. M., van Spronsen, M. A., Madix, R. J. & Friend, C. M. O_2 activation by metal surfaces: implications for bonding and reactivity on heterogeneous catalysts. *Chem. Rev.* **118**, 2816–2862 (2017).
9. Zhou, J. et al. Boridene: two-dimensional $Mo_{4/3}B_{2-x}$ with ordered metal vacancies obtained by chemical exfoliation. *Science* **373**, 801–805 (2021).
10. Kim, S. J. et al. Flat-surface-assisted and self-regulated oxidation resistance of Cu(111). *Nature* **603**, 434–438 (2022).
11. Ai, M. H. et al. Spin selection in atomic-level chiral metal oxide for photocatalysis. *Nat. Commun.* **14**, 4562 (2023).
12. Lin, C. C. et al. Spin-polarized photocatalytic CO_2 reduction of Mn-doped perovskite nanoplates. *J. Am. Chem. Soc.* **144**, 15718–15726 (2022).
13. Yang, B. B. et al. Engineering relaxors by entropy for high energy storage performance. *Nat. Energy* **8**, 956–964 (2023).
14. McDougall, N. L., Nicholls, R. J., Partridge, J. G. & McCulloch, D. G. The near edge structure of hexagonal boron nitride. *Microsc. Microanal.* **20**, 1053–1059 (2014).
15. Paris, E. et al. Strain engineering of the charge and spin–orbital interactions in Sr_2IrO_4. *Proc. Natl Acad. Sci. USA* **117**, 24764–24770 (2020).
16. Liu, Z. et al. A conductive network and dipole field for harnessing photogenerated charge kinetics. *Adv. Mater.* **33**, 2104099 (2021).
17. Zhu, H. et al. Dual interfacial electric fields in black phosphorus/MXene/MBene enhance broad-spectrum carrier migration efficiency of photocatalytic devices. *Device* **2**, 2666–9986 (2024).
18. Chen, F. et al. Identification of the stable Pt single sites in the environment of ions: from mechanism to design principle. *Adv. Mater.* **34**, 2108504 (2022).
19. Liu, J. C., Luo, F. & Li, J. Electrochemical potential-driven shift of frontier orbitals in M–N–C single-atom catalysts leading to inverted adsorption energies. *J. Am. Chem. Soc.* **145**, 25264–25273 (2023).
20. Huang, P. et al. Dynamic orbital hybridization triggered spin-disorder renormalization via super-exchange interaction for oxygen evolution reaction. *Proc. Natl Acad. Sci. USA* **120**, e2219661120 (2023).
21. Lee, A. S. et al. Methicillin-resistant *Staphylococcus aureus*. *Nat. Rev. Dis. Prim.* **4**, 1–23 (2018).
22. Larsen, J. et al. Emergence of methicillin resistance predates the clinical use of antibiotics. *Nature* **602**, 135–141 (2022).
23. Schlievert, P. M., Strandberg, K. L., Lin, Y. C., Peterson, M. L. & Leung, D. Y. Secreted virulence factor comparison between methicillin-resistant and methicillin-sensitive *Staphylococcus aureus*, and its relevance to atopic dermatitis. *J. Allergy Clin. Immunol.* **125**, 39–49 (2010).
24. Zheng, X. et al. The cell envelope of *Staphylococcus aureus* selectively controls the sorting of virulence factors. *Nat. Commun.* **12**, 6193 (2021).
25. Peetermans, M., Verhamme, P. & Vanassche, T. Coagulase activity by *Staphylococcus aureus*: a potential target for therapy? *Semin. Thromb. Hemost.* **41**, 433–444 (2015).
26. McAdow, M., Missiakas, D. M. & Schneewind, O. *Staphylococcus aureus* secretes coagulase and von Willebrand factor binding protein to modify the coagulation cascade and establish host infections. *J. Innate Immun.* **4**, 141–148 (2012).
27. Li, J. et al. 2D MOF periodontitis photodynamic ion therapy. *J. Am. Chem. Soc.* **143**, 15427–15439 (2021).
28. Wang, R. et al. Graphdiyne-modified TiO_2 nanofibers with osteoinductive and enhanced photocatalytic antibacterial activities to prevent implant infection. *Nat. Comm.* **11**, 4465 (2020).
29. Hong, Y., Zeng, J., Wang, X., Drlica, K. & Zhao, X. Post-stress bacterial cell death mediated by reactive oxygen species. *Proc. Natl Acad. Sci. USA* **116**, 10064–10071 (2019).
30. Liu, Z. et al. Work function mediated interface charge kinetics for boosting photocatalytic water sterilization. *J. Hazard. Mater.* **442**, 0304–3894 (2023).
31. Akiyama, H., Ueda, M., Kanzaki, H., Tada, J. & Arata, J. Biofilm formation of *Staphylococcus aureus* strains isolated from impetigo and furuncle: role of fibrinogen and fibrin. *J. Dermatol. Sci.* **16**, 2–10 (1997).
32. Maree, M. et al. Natural transformation allows transfer of SCC*mec*-mediated methicillin resistance in *Staphylococcus aureus* biofilms. *Nat. Commun.* **13**, 2477 (2022).
33. McKellar, S. W. et al. RNase III CLASH in MRSA uncovers sRNA regulatory networks coupling metabolism to toxin expression. *Nat. Commun.* **13**, 3560 (2022).
34. Wang, Z. J. et al. Natural carrier-free binary small molecule self-assembled hydrogel synergize antibacterial effects and promote wound healing by inhibiting virulence factors and alleviating the inflammatory response. *Small* **19**, 2205528 (2022).
35. Tan, H. et al. Photocatalysis of water into hydrogen peroxide over an atomic Ga-N_5 site. *Nat. Synth.* **2**, 557–563 (2023).
36. Liu, C., Xu, W. Z. & Charpentier, P. A. Synthesis and photocatalytic antibacterial properties of Poly[2,11′-thiopheneethylenethiophene-alt-2,5-(3-carboxyl)thiophene]. *ACS Appl. Polym. Mater.* **2**, 1886–1896 (2020).
37. Liu, N. et al. Sustainable photocatalytic disinfection of four representative pathogenic bacteria isolated from real water environment by immobilized TiO_2-based composite and its mechanism. *Chem. Eng. J.* **426**, 131217 (2021).

38. Yan, H. et al. Binary composite MoS_2/TiO_2 nanotube arrays as a recyclable and efficient photocatalyst for solar water disinfection. *Chem. Eng. J.* **401**, 126052 (2020).
39. Brindha, B. et al. Dynamic Ag-mediated electron transfer confined ZnO nanorods for boosted photocatalytic bacterial disinfection. *J. Clean. Prod.* **451**, 141908 (2024).
40. Jiang, Z. et al. Solar-light-driven rapid water disinfection by ultrathin magnesium titanate/carbon nitride hybrid photocatalyst: band structure analysis and role of reactive oxygen species. *Appl. Catal. B* **257**, 117898 (2019).
41. Fouad, M. et al. Visible-light-driven photocatalytic disinfection of raw surface waters (300–5000 CFU/mL) using reusable coated Ru/WO_3/ZrO_2. *J. Hazard. Mater.* **402**, 123514 (2021).
42. Xu, J., Wang, Z. & Zhu, Y. Highly efficient visible photocatalytic disinfection and degradation performances of microtubular nanoporous g-C_3N_4 via hierarchical construction and defects engineering. *J. Mater. Sci. Technol.* **49**, 133–143 (2020).
43. Yang, T. et al. Visible light-driven D-A conjugated linear polymer and its coating for dual highly efficient photocatalytic degradation and disinfection. *ACS Appl. Mater. Interfaces* **13**, 51447–51458 (2021).
44. Pham, N.-D. et al. Photocatalytic disinfection of *E. coli* using silver-doped TiO_2 coated on cylindrical cordierite honeycomb monolith photoreactor under artificial sunlight irradiation. *Top. Catal.* **66**, 75–88 (2022).
45. Zeng, Z. et al. Energy-transfer-mediated oxygen activation in carbonyl functionalized carbon nitride nanosheets for high-efficient photocatalytic water disinfection and organic pollutants degradation. *Water Res.* **177**, 115798 (2020).
46. Liao, Y., Wang, J., Song, X., Zhang, G. & Chen, B. Low-cost and large mass producible phenolic resin for water disinfection and antibacterial coating under weak visible light LED or sunlight irradiation. *Appl. Catal. B* **292**, 120189 (2021).
47. Yang, Y. Y. et al. Appropriate oxygen vacancies and Mo–N bond synergistically modulate charge transfer dynamics of MoO_{3-x}/S-CN for superior photocatalytic disinfection: unveiling synergistic effects and disinfection mechanism. *J. Hazard. Mater.* **445**, 130481 (2023).
48. Xu, X. et al. Visible-light photocatalysis of organic contaminants and disinfection using biomimetic-synthesized TiO_2–Ag–AgCl composite. *Appl. Surf. Sci.* **588**, 152886 (2022).
49. Liu, H. et al. Defective engineering in graphitic carbon nitride nanosheet for efficient photocatalytic pathogenic bacteria disinfection. *Appl. Catal. B* **261**, 118201 (2020).
50. Yan, T., Huang, J., Bi, J., Xie, L. & Huang, H. Preparation of $Ga_{0.25}Zn_{4.67}S_{5.08}$ microsphere by ultrasonic spray pyrolysis and its photocatalytic disinfection performance under visible light. *J. Nanomater.* **2019**, 1–9 (2019).
51. Yang, X. et al. Carbon dots cooperatively modulating photocatalytic performance and surface charge of O-doped g-C_3N_4 for efficient water disinfection. *J. Colloid Interface Sci.* **631**, 25–34 (2023).
52. Yu, P., Zhou, X., Yan, Y., Li, Z. & Zheng, T. Enhanced visible-light-driven photocatalytic disinfection using AgBr-modified g-C_3N_4 composite and its mechanism. *Colloids Surf. B* **179**, 170–179 (2019).
53. Che, S. et al. Construction of a 2D layered phosphorus-doped graphitic carbon nitride/BiOBr heterojunction for highly efficient photocatalytic disinfection. *Chem. Asian J.* **17**, e202200095 (2022).
54. Zhang, S. et al. Fast and universal solution-phase flocculation strategy for scalable synthesis of various few-layered MXene powders. *J. Phys. Chem. Lett.* **11**, 1247–1254 (2020).
55. Wang, V., Xu, N., Liu, J.-C., Tang, G. & Geng, W.-T. VASPKIT: a user-friendly interface facilitating high-throughput computing and analysis using VASP code. *Comput. Phys. Commun.* **267**, 0010–4655 (2021).
56. Maintz, S., Deringer, V. L., Tchougréeff, A. L. & Dronskowski, R. LOBSTER: a tool to extract chemical bonding from plane-wave based DFT. *J. Comput. Chem.* **37**, 1030–1035 (2016).

Acknowledgements

We thank the National Key Research and Development Program of China (Nos. 2023YFE0103300 and 2021YFA1202500), the Innovative Talent Promotion Program-Science & Technology Innovation Team of Shaanxi (2023-CX-TD-55), the National Natural Science Foundation of China (Nos. 52270053 and 22422604), National Science Fund for Distinguished Young Scholars (No. 52025133), the Beijing Nova Program (No. 20220484215) and the Beijing Natural Science Foundation (No. 8232035). The authors would also like to thank Guoyun Zhang (State Key Laboratory of Crop Stress Biology for Arid Areas, Northwest A&F University, China) for their technical assistance. Supports from the Beamlines MCD-B (Soochow Beamline for Energy Materials) and Fourier transform infrared spectrometer (Bruker IFS 66v) on the infrared beamline (BL01B) at National Synchrotron Radiation Laboratory (NSRL) of China, Shanghai Synchrotron Radiation Facility (Instrument BL11B), the 1W1B station at Beijing Synchrotron Radiation Facility (BSRF), the High-Performance Computing Platform of Peking University and Analytical Testing Center of School of Environmental Science and Engineering of Shandong University, are also greatly acknowledged.

Author contributions

S.G., J.W., W.L., and Y.S. conceived the project. Z.L. and W.G. carried out most of the materials fabrication and characterization and prepared the manuscript. Z.L., L.L. (Lizhi Liu), Y.G., C. Z.L.C., and F.L. performed the partial experiments and theoretical calculations. Z.L., W.G., J.X., T.D., L.L. (Linpin Luo) and J.Z. conducted the operando EPR measurements. Z.L., W.Z., Y.J., and M.L. conducted part of the photocatalytic sterilization tests. All authors discussed the results and commented on the manuscript.

Competing interests

The authors declare no competing interests.

Inclusion and Ethics statement

All animal procedures were performed in accordance with the Guidelines for Care and Use of Laboratory Animals and experiments were approved by the Animal Ethics Committee of Northwest A&F University.

Additional information

Supplementary information The online version contains supplementary material available at https://doi.org/10.1038/s41467-024-55626-8.

Correspondence and requests for materials should be addressed to Yizhong Shen, Wen Liu, Jianlong Wang or Shaojun Guo.

Peer review information *Nature Communications* thanks Guangfu Liao, Houjuan Zhu and the other, anonymous, reviewer for their contribution to the peer review of this work. A peer review file is available.